Development of an Aerodynamic Simulation Technique Based on the Vortex Particle Method

Johan Valentin, Rocco Moretti, Luis Bernardos

Development of an Aerodynamic Simulation Technique Based on the Vortex Particle Method

Johan VALENTIN, Rocco Moretti, Luis Bernardos

ONERA, DAAA, Université Paris-Saclay, Meudon, 92190, France

johan.valentin@onera.fr

Abstract

The study detailed in this paper aims to provide a solver able to simulate of a complex flows with multiple unsteady interactions. The numerical application of vortex methods has been studied intensively during the second half of the 20^{th} century. In particular, the Vortex Particle Method (VPM), aims to represent an incompressible flow through singular particles. However, its computational cost curtailed its use until recently. Since each particle influences one another, the VPM cost is $\mathcal{O}(N_p^2)$, with N_p the number of particles. Fortunately enough, recent methods can be used to accelerate such problems to make it a $\mathcal{O}(N)$ problem. After introducing the VPM, its implementation and acceleration are detailed. A validation of the algorithm is conducted on several test cases. In addition, a comparison with other similar studies is carried out to validate its robustness and accuracy. Eventually a lifting line is added to study the reaction of the VPM when confronted with a wing.

Keywords: Aerodynamic Simulation, Vortex Particle, Vortex Ring, Lifting Line, Fast Multipole Method

Nomenclature

α_{rel}	Relative AoA $[rad]$	E	Kinetic Energy $[m^5.s^{-2}]$	ϕ	Curl-Free Potential $[m^2.s^{-1}]$
$\overrightarrow{\alpha}$	Vorticity Strength $[m^3.s^{-1}]$	F	Total Lift $[N]$	ρ	Dimensionless Distance
$\overrightarrow{\mathcal{A}}$	Angular Impulse $[m^5.s^{-1}]$	Γ	Circulation $[m^2.s^{-1}]$	R	Ring Radius $[m]$
a	Radius of Ring Section $[m]$	$\mathcal{H}$	Helicity $[m^4.s^{-2}]$	σ	Particle Core Radius $[m]$
b	Wingspan $[m]$	h	Resolution Length $[m]$	$\overrightarrow{u_\infty}$	FreeStream Velocity $[m.s^{-1}]$
c	Chord $[m]$	$\overrightarrow{\mathcal{I}}$	Linear Impulse $[m^4.s^{-1}]$	$\overrightarrow{u_{rel}}$	Relative Velocity $[m.s^{-1}]$
C_l, C_d	2D Lift and Drag Coefficient	$\overrightarrow{L}$	Lift $[N]$	$\overrightarrow{u}$	Induced Velocity $[m.s^{-1}]$
c_L, c_D	3D Lift and Drag Coefficient	k_{relax}	Circulation Relaxation	V	Volume of the Particle $[m^3]$
c_s	Smagorinski Constant	ν	Kinematic Viscosity $[m^2.s^{-1}]$	$\overrightarrow{\Omega}$	Total Vorticity $[m^3.s^{-1}]$
$\overrightarrow{D}$	Drag $[N]$	N_p	Number of Particles	$\overrightarrow{\omega}$	Vorticity $[s^{-1}]$
ϵ	Induced Angle $[rad]$	N_s	Number of Sources	w	Downwash $[m.s^{-1}]$
$\mathcal{E}$	Enstrophy $[m^3.s^{-2}]$	$\overrightarrow{\psi}$	Div-Free Potential $[m^2.s^{-1}]$	$\overrightarrow{x_i}$	Particle Position $[m]$

I Introduction

New concepts of eVTOL (electric Vertical Takeoff and Landing) vehicles have spread during the last decade. The use of several rotors generates a strong propulsion allowing vertical take off and precise handling of the vehicle. The aerodynamic interactions between several rotors are arduous to accurately simulate with low fidelity methods and they are also too costly to be studied with high fidelity methods (CFD). This is especially the case during the design phase. The need for a fast and accurate method, which can fully take into account the interactions between multiple rotors, motivated this study.

High-fidelity CFD methods remain computationally costly and fail to be used in industrial design process. The Vortex Particle Method (VPM) was developed here to tackle this challenge. This potential method, first introduced by Rosenhead in 1931[13], aims to represent continuous unsteady flows through the use of singular particles. Since then various authors managed to use this method to simulate: propeller-on-wing interactions[4], rotors in hover configuration with a Lifting Line[6], rotor wake transition and coplanar rotors wake mixing[1], marine turbines with a panel method[12]... This incompressible method is particularly well suited to represent wake decay and mixing, and viscous effects where other panel or filament methods fail to do so, making it a possible candidate to simulate the interactions between the wakes of several different rotors. Moreover, It is also a meshless method which significantly reduces computational dissipation.

The goal of this study is to create a new algorithm from scratch based on the VPM. This code will have a Python interface while running in C++. The solver has been developed into the ONERA CASSIOPEE (CFD Advanced Set of Services In an Open Python EnvironmEnt)[3] environment of ONERA which uses the CGNS standard (CFD General Notation System). The validation with well-known case studies will then be carried out to validate the algorithm. Eventually, a Lifting Line (LL) method will be coupled to the solver in order to simulate a wing.

II 3D Viscous Vortex Particle Method

II.1 Modelisation of the VPM

The VPM is a vortex method and, as such, aims to represent the flow through its vorticity $\overrightarrow{\omega}(\vec{x},t) = \nabla \times \overrightarrow{u}(\vec{x},t)$. This method uses singular particles to represent a continuous flow. The particles can move freely (as opposed to prescribed-wake approaches) and influence each other. To follow the evolution of the particles, the Lagrangian representation of the flow is adopted. To do so, the vorticity equation is used. It is obtained by taking the curl of the traditional three-dimensional Navier-Stokes equations for a viscous and incompressible flow:

$$\frac{\mathrm{d}\overrightarrow{\omega}}{\mathrm{d}t} = \left(\overrightarrow{\omega}\cdot\nabla\right)\overrightarrow{u} + \nu\nabla^2\overrightarrow{w} \qquad (1)$$

where 1^{st} term on the RHS accounts for the stretching and compression between particles while the 2^{nd} term allows for reconnection and diffusion. One has also $\left(\overrightarrow{\omega}\cdot\left({}^t\nabla - \nabla\right)\right)\overrightarrow{u} = \overrightarrow{\omega}\times\left(\nabla\times\overrightarrow{u_i}\right) = \overrightarrow{\omega}\times\overrightarrow{\omega} = \overrightarrow{0}$ which leads to write the 1^{st} term as $\left(\overrightarrow{\omega}\cdot{}^t\nabla\right)\overrightarrow{u}$. It has been

shown that this representation is the only one to conserve the total vorticity of the flow[17]. For this reason, this scheme will be the one used for this study.

Each particle is a vector element represented by a position ($\vec{x_i}$), a core size (σ), a volume (V_i) and a strength ($\overrightarrow{\alpha_i} \approx V_i \overrightarrow{\omega_i}$). The vorticity field is discretized as follows:

$$\overrightarrow{\omega_i}(\overrightarrow{x_i}, t) = \sum_{p=1}^{N_p} \delta(\overrightarrow{x_i} - \overrightarrow{x_p}) \overrightarrow{\alpha_p}(t) \tag{2}$$

The velocity of the particles is then obtained thanks to the Helmholtz Decomposition Theorem:

$$\frac{\mathrm{d}\vec{x}_i}{\mathrm{d}t} = \overrightarrow{u_\infty} + \nabla \times \overrightarrow{\psi} + \nabla\phi \tag{3}$$

where $\nabla\phi$ is the velocity induced by a lifting surface and $\overrightarrow{u} = \nabla \times \overrightarrow{\psi}$ is induced by the particles. The vorticity and velocity are then linked by the latter streamfunction:

$$\overrightarrow{\omega} = \nabla \times (\nabla \times \overrightarrow{\psi}) = \nabla \left(\cancelto{0}{\nabla \cdot \overrightarrow{\psi}} \right) - \nabla^2 \overrightarrow{\psi} \tag{4}$$

The solution of a Poisson's equation is given by Green's function:

$$\overrightarrow{\psi}(\overrightarrow{x}, t) = \int_V G(\overrightarrow{x}, \overrightarrow{x}') \overrightarrow{\omega}(\overrightarrow{x}', t) d\overrightarrow{x}' \tag{5}$$

$$\approx \sum_{p=1}^{N_p} G(\overrightarrow{x}, \overrightarrow{x_p}) \overrightarrow{\alpha_p}(t) \tag{6}$$

Finally, the velocity is obtained by taking the curl of the previous equation:

$$\overrightarrow{u_i}(\overrightarrow{x_i}, t) = \sum_{p=1}^{N} K(\overrightarrow{x_i} - \overrightarrow{x_p}) \times \overrightarrow{\alpha_p}(t) \tag{7}$$

where $K(\overrightarrow{x_i} - \overrightarrow{x_p}) = \frac{-1}{4\pi ||\overrightarrow{x_i} - \overrightarrow{x_p}||^3} (\overrightarrow{x_i} - \overrightarrow{x_p})$ is the Biot-Savart kernel.

II.2 Regularisation of the Particles

In order to avoid singularities when particles get close, a function g is used to regularise the previous kernel:

$$K(\vec{x}) = -\frac{g(\rho)}{|\vec{x}|^3} \vec{x} \tag{8}$$

where $\rho = \frac{|\vec{x}|}{\sigma}$.

The viscous term of the vorticity equation can not be calculated as it is, because the strength of the particles is not a function of space. The Particle Strength Exchange (PSE) [10][17][15][6] is nonetheless used to account for the viscous effects of the fluid:

$$\nabla^2 \overrightarrow{\omega}(\vec{x}) \approx 2 \int_V \eta(\vec{x} - \vec{x}') [\overrightarrow{\omega}(\vec{x}') - \overrightarrow{\omega}(\vec{x})] d\vec{x}' \tag{9}$$

$$\nu \nabla^2 \overrightarrow{\alpha_i} \approx \sum_{p=1}^{N_p} \frac{\nu_i + \nu_p}{2} \eta(\vec{x}_i - \vec{x}_p) [V_i \overrightarrow{\alpha_p} - V_p \overrightarrow{\alpha_i}] \tag{10}$$

The η function can be directly linked with the regularisation function used with the Biot-Savart kernel:

$$\eta(\rho) = \frac{1}{\sigma^5 \rho^4} \left(2 \frac{\mathrm{d}g(\rho)}{\mathrm{d}\rho} - \rho \frac{\mathrm{d}^2 g(\rho)}{\mathrm{d}\rho^2} \right) \tag{11}$$

However, it has been observed that the diffusion term of the vorticity equation is often negligible in front of the stretching term, especially when considering air flows ($\nu \approx 1.56 \cdot 10^{-5} m^2.s^{-1}$). In order to better take into account the viscous effects of the flow, a turbulent viscosity is added to the kinematic viscosity:

$$\nu = \nu_{air} + (C_s \sigma)^2 \sqrt{2} ||\overrightarrow{\omega}|| \tag{12}$$

This model is taken from the Smagorinski model[8]. To better represent the diffusion term, it is necessary to stabilise the regions of the flow where the vorticity gets carried away.

The Smagorinski constant is the same as the one from the LES model and is usually taken between 0.15 and 0.25.

Both Gaussian and High Order Algebraic (HOA) regularisation kernels have been implemented (see Table:1). They only differ by the fact that the HOA regularisation smoothes less when particles are close.

Kernels	$g(\rho)$
HOA	$\frac{1}{4\pi}\frac{\rho^3(\rho^2+5/2)}{(\rho^2+1)^{5/2}}$
Gaussian	$\frac{1}{4\pi}\left(\text{erf}\left(\frac{\rho}{\sqrt{2}}\right)-\sqrt{\frac{2}{\pi}}\rho e^{-\frac{\rho^2}{2}}\right)$

Table 1: *Regularisation Functions.*

The fully regularised system to solve becomes:

$$\frac{\mathrm{d}\overrightarrow{x_i}(t)}{\mathrm{d}t} = \overrightarrow{u}_\infty + \sum_{p=1}^{N} -\frac{1}{\sigma^3}\frac{g(\rho)}{\rho^3}(\vec{x}_i-\vec{x}_p)\times\overrightarrow{\alpha_p} \quad (13)$$

$$\frac{\mathrm{d}\overrightarrow{\alpha_i}(t)}{\mathrm{d}t} = \sum_{p=1}^{N_p}\Bigg[\frac{1}{\sigma^3}\frac{g(\rho)}{\rho^3}\overrightarrow{\alpha_i}\times\overrightarrow{\alpha_p}$$

$$+\frac{1}{\sigma^5\rho}\frac{\mathrm{d}}{\mathrm{d}\rho}\left(\frac{g(\rho)}{\rho^3}\right)(\overrightarrow{\alpha_i}\cdot((\vec{x}_i-\vec{x}_p)\times\overrightarrow{\alpha_p})(\vec{x}_i-\vec{x}_p)$$

$$+\frac{\nu_i+\nu_p}{\sigma^5\rho^4}\left(2\frac{\mathrm{d}g(\rho)}{\mathrm{d}\rho}-\rho\frac{\mathrm{d}^2g(\rho)}{\mathrm{d}\rho^2}\right)(V_i\overrightarrow{\alpha_p}-V_p\overrightarrow{\alpha_i})\Bigg] \quad (14)$$

A 1^{st}, 2^{nd} and 3^{rd} order Runge Kutta schemes were implemented to solve this system. Beale, Majda[2] and Greengard[5] proved the convergence of this regularisation as long as $1 < \frac{\sigma}{h}$; where h represents the typical distance between particles and σ the core size of the particles.

The vorticity of the particles can be obtained by the VPM by also regularising the Dirac delta function. The function $\zeta(\rho) = \frac{1}{\rho^2}\frac{\mathrm{d}g(\rho)}{\mathrm{d}\rho}$ has been applied:

$$\overrightarrow{\omega_i} = \sum_{p}^{N_p}\frac{\zeta(\rho)}{\sigma^3}\overrightarrow{\alpha}_p \quad (15)$$

The vorticity used for the post-treatment however is obtained from the velocity induced by the particles on a Cartesian grid.

II.3 Other Schemes

The major drawback of this approach is that even though the velocity is divergence-free, it is not necessarily the case of the vorticity[17]. Pedrizzetti's relaxation scheme has been implemented to address this issue[11]. The scheme aims to realign the particles' strength with their vorticity:

$$\overrightarrow{\alpha}_{new} = (1-f\Delta t)\overrightarrow{\alpha}_{old} + f\Delta t\frac{\overrightarrow{\omega_{old}}}{|\overrightarrow{\omega_{old}}|}|\overrightarrow{\alpha}_{old}| \quad (16)$$

where f is a cutoff frequency to be tuned with the simulation.

To address any Lagrangian distortion, a global redistribution of the particles' strength has also been implemented. This allows to project the strength of all particles on a Cartesian grid of mesh size h, built of the orthonormal base $(\vec{e}_1, \vec{e}_2, \vec{e}_3)$ like represented in Figure 1. This way the strength at a node j is:

$$\overrightarrow{\alpha_j} = \sum_{p=1}^{N_p}\left[\prod_{k=1}^{3}M_4'\left(\frac{||(\vec{x}_j-\vec{x}_p).\vec{e}_k||}{h}\right)\right]\overrightarrow{\alpha_p} \quad (17)$$

where:

$$M_4' = \begin{cases} 1-\frac{5}{2}\rho^2+\frac{3}{2}|\rho|^3 & \text{, if } \quad 0\le|\rho|\le 1 \\ \frac{1}{2}(1-|\rho|)(2-|\rho|)^2 & \text{, if } \quad 1\le|\rho|\le 2 \\ 0 & \text{, if } \quad 2\le|\rho| \end{cases}$$

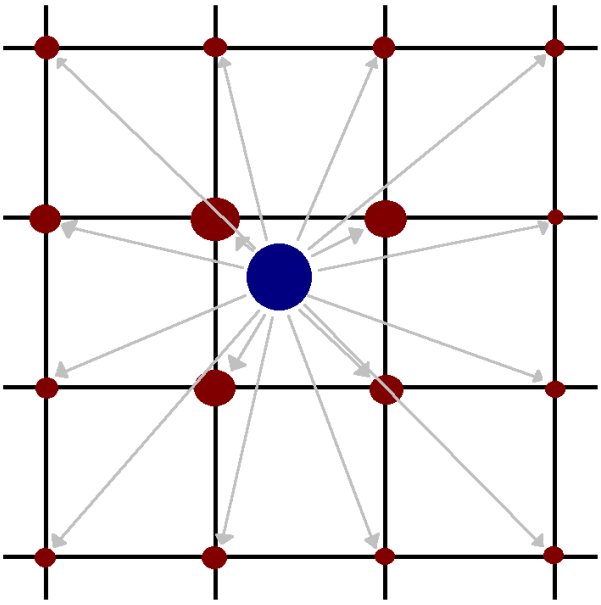

Fig. 1: *Example of Global Redistribution on a 2D lattice.*

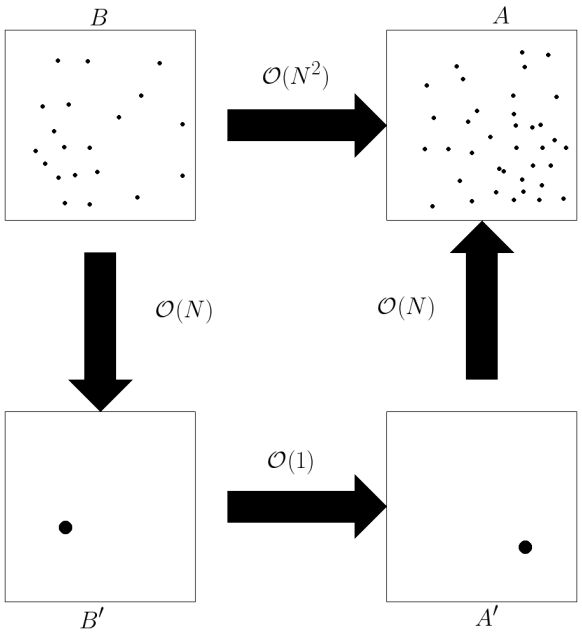

Fig. 2: *Concept of the FMM.*

II.4 Acceleration Method

In its current state, the VPM remains costly. The inter-particular interactions makes it a $\mathcal{O}(N^2)$ problem, preventing from efficiently using more than 10^4 particles. In order to reduce computing costs, the Fast Multipole Method (FMM) module ExaFMM[18] has been fully optimised, parallelised, vectorised and implemented into the solver. This method aims to separate particles into clusters as shown in Figure 2. Interactions between two clusters far apart can be summed up as a single interaction, thus reducing inter-particular interactions to particles close to each other. In best case scenarii, the VPM becomes a $\mathcal{O}(N)$ problem.

III Vortex Rings

This section describes the validation of the VPM, without vorticity sources, on vortex rings configurations.

III.1 Conservation Laws

The behaviour of the VPM can be assessed through the monitoring of conservation laws. The linear invariants are the Total Vorticity ($\overrightarrow{\Omega}$), Linear Impulse ($\overrightarrow{\mathcal{I}}$) and Angular Impulse ($\overrightarrow{\mathcal{A}}$) while the quadratic invariants are the kinetic energy (E), the Enstrophy ($\mathcal{E} = -1/\nu \frac{\mathrm{d}E}{\mathrm{d}t}$) and the Helicity ($\mathcal{H}$). The analytical solutions of the linear diagnostics are fairly easy to obtain with regularised quantities though it is not the case for the quadratic ones. Winckelmans still managed to obtain a solution by semi-regularising the diagnostics with the HOA[17]:

$$\overrightarrow{\Omega} = \sum_{p=1}^{N_p} \overrightarrow{\alpha_p} \tag{18}$$

$$\overrightarrow{\mathcal{I}} = \frac{1}{2}\sum_{p=1}^{N_p} \vec{x}_p \times \overrightarrow{\alpha_p} \tag{19}$$

$$\overrightarrow{\mathcal{A}} = \frac{1}{3}\sum_{p=1}^{N_p} \vec{x}_p \times (\vec{x}_p \times \overrightarrow{\alpha_p}) \tag{20}$$

$$E = \frac{1}{16\pi}\sum_{p,q=1}^{N_p}\Bigg[\frac{1}{(|\vec{x}_p-\vec{x}_q|^2+\sigma^2)^{3/2}}\cdot \Big((|\vec{x}_p-\vec{x}_q|^2+2\sigma^2)\overrightarrow{\alpha_p}\cdot\overrightarrow{\alpha_q} + ((\vec{x}_p-\vec{x}_q)\cdot\overrightarrow{\alpha_p})((\vec{x}_p-\vec{x}_q)\cdot\overrightarrow{\alpha_q})\Big)\Bigg] \tag{21}$$

$$\mathcal{E} = \frac{1}{4\pi}\sum_{p,q=1}^{N_p}\Bigg[\frac{10\sigma^4+\frac{7}{2}\sigma^2|\vec{x}_p-\vec{x}_q|^2+|\vec{x}_p-\vec{x}_q|^4}{(|\vec{x}_p-\vec{x}_q|^2+\sigma^2)^{7/2}}\overrightarrow{\alpha_p}\cdot\overrightarrow{\alpha_q} - \frac{3}{2}\frac{7\sigma^4+9\sigma^2|\vec{x}_p-\vec{x}_q|^2+2|\vec{x}_p-\vec{x}_q|^4}{(|\vec{x}_p-\vec{x}_q|^2+\sigma^2)^{9/2}}\cdot ((\vec{x}_p-\vec{x}_q)\cdot\overrightarrow{\alpha_p})((\vec{x}_p-\vec{x}_q)\cdot\overrightarrow{\alpha_q})\Bigg] \tag{22}$$

Another formulation of E and $\mathcal{E}$ can be obtained with the hypothesis of a purely divergence-free flow. This can help monitor the divergence of the flow by evaluating the difference between both diagnostics ($|E - E_{div-free}|$ and $|\mathcal{E} - \mathcal{E}_{div-free}|$).

III.2 Rings Initialisation

Vortex rings were computed in order to be compared with other studies and well-known experiences. Those torus-shaped rings were modeled following the geometry given by Knio and Ghoniem[7]. The section of the ring is a disk composed of several concentric layers of particles. These layers can go beyond a, the radius of the ring's section to represent the flow around the rings. This radius is taken as $a \ll R$ so that the ring remains thin. Eventually the particles are initialised as proposed by Winckelmans:

$$\overrightarrow{\omega}(t=0) = \frac{\Gamma}{2\pi a^2}\left(1+\frac{r}{R}\cos\theta\right)e^{-\frac{r^2}{2a^2}}\vec{e}_\psi \tag{23}$$

The strength of the particles is obtained by solving $A[\overrightarrow{\alpha}_i] = [\overrightarrow{\omega}_i]$ where the square matrix A contains the values of $A_{ij} = \zeta\left(\frac{||\vec{x}_i-\vec{x}_j||}{\sigma}\right)$.

III.3 The Self-Induced Ring

A vortex ring is a toroidal-shaped ring with a concentration of vorticity in its section core. Such rings can translate solely due to their self induction. A single self-induced ring is simulated and compared with other studies. The HOA regularisation was used to stay consistent with the other authors. The diagnostics obtained by the solver and from other studies are compared in Table:2. While the diagnostics remain close, the temporal rate of change of E which is different than Singh's. This could be explained by the difference of integrating scheme or the way the matricial system is solved to obtain the particles' strength.

Knowing $\overrightarrow{\omega}(t=0)$, one can calculate $\mathcal{E}(t=0) = 50.75m^3s^{-1}$. The difference between the computed and analytical values could come from the semi-regularisation used[17]. Nevertheless the diagnostics can still be used as a mean to check the divergence of the simulations.

The evolution of the diagnostics has also been compared to the ones of Winckelmans' in Figure 3 to 8. In the viscous case, the rate of change of the kinetic energy is close to variation of the Enstrophy, as predicted by $dE/dt = -\nu\mathcal{E}$ in Figure 5. The curvature of the kinetic energy at around $\approx 2s$ also shows that the vorticity of the ring concentrated at its core has been diffused to its last layer thanks to the PSE. The inviscid case shows in turn the conservation of kinetic energy. The linear diagnostics are all conserved as is expected for an unbounded, divergence-free, source-less simulation.

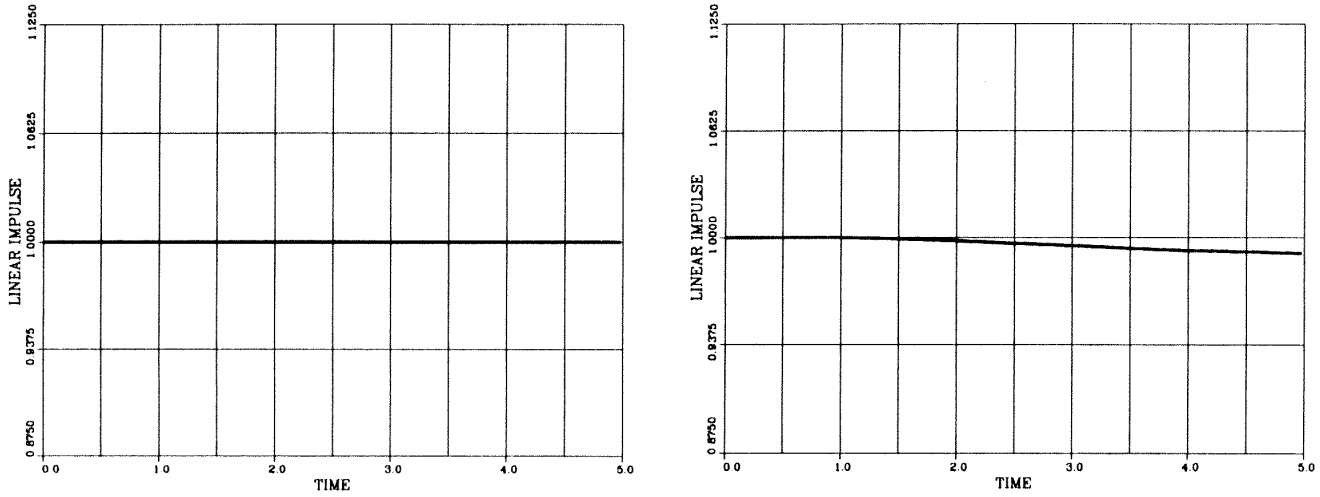

Fig. 3: *Linear Impulse for an Inviscid (left) and Viscous (right) Vortex Ring by Winckelmans[17].*

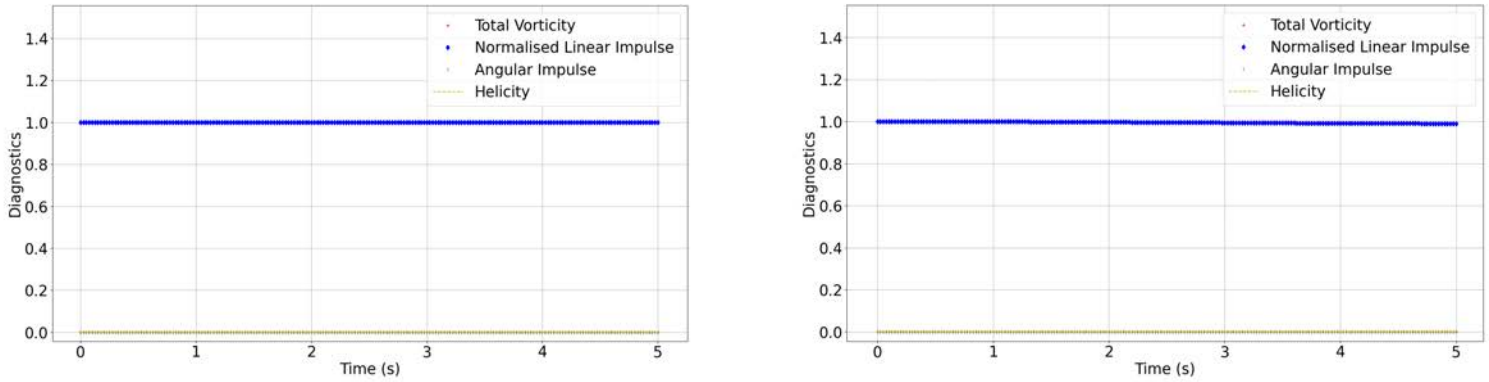

Fig. 4: *Linear Diagnostics for an Inviscid (left) and Viscous (right) Vortex Ring.*

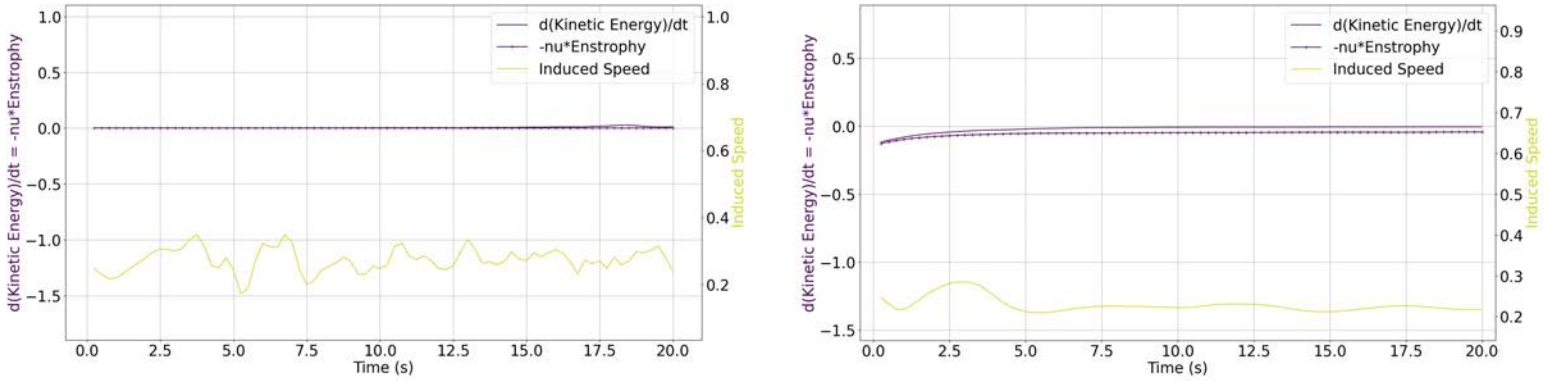

Fig. 5: *Velocity and Kinetic Energy Variation for an Inviscid (left) and Viscous (right) Vortex Ring.*

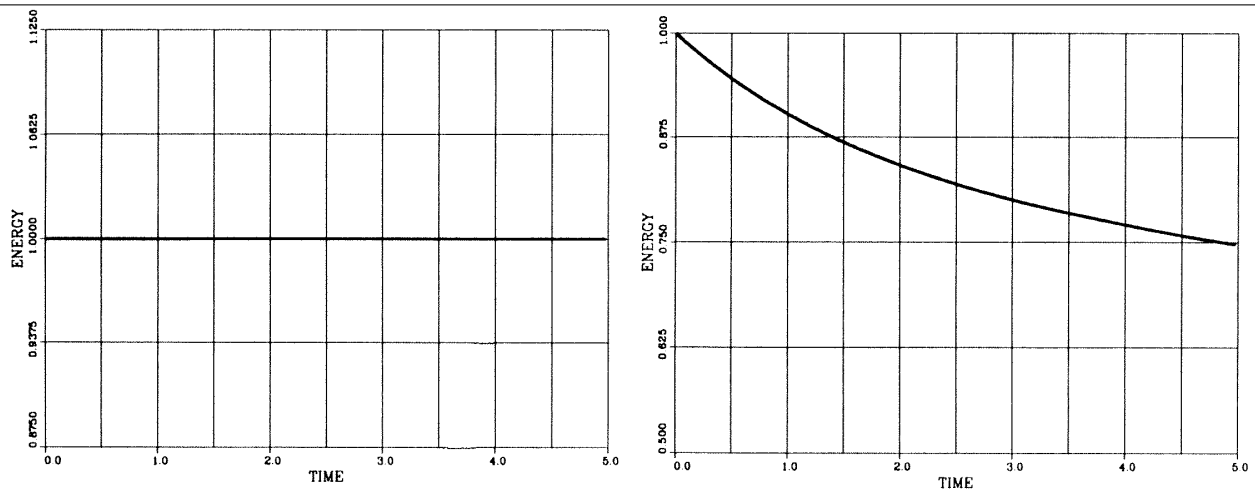

Fig. 6: *Kinetic Energy for an Inviscid (left) and Viscous (right) Vortex Ring by Winckelmans[17].*

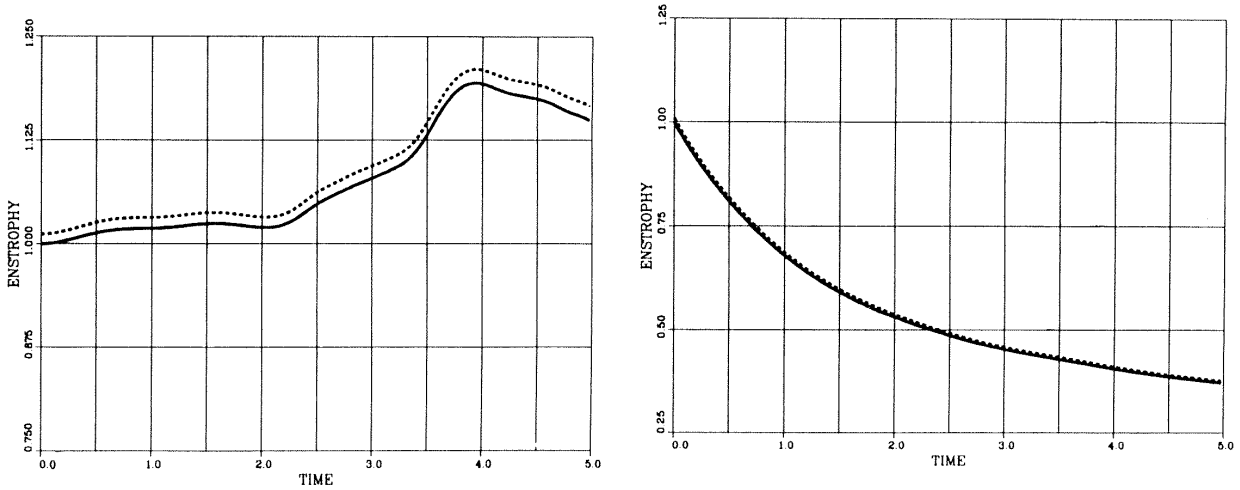

Fig. 7: *Enstrophy for an Inviscid (left) and Viscous (right) Vortex Ring by Winckelmans[17].*

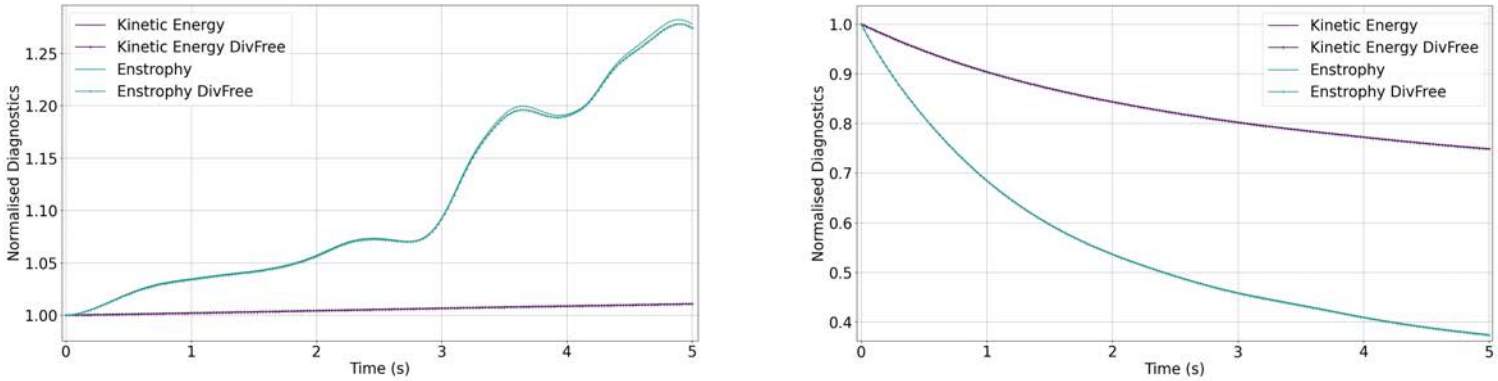

Fig. 8: *Kinetic Energy and Enstrophy for an Inviscid (left) and Viscous (right) Vortex Ring.*

III.4 Leap-Frogging Rings

The leap-frog phenomenon shows that when two rings follow each another, the one behind will tend to contract and accelerate while the one in front will loosen up and decelerate. This leads to the ring behind to go through the one in front. This operation is repeated in a back-and-forth fashion. The goal is to reenact this phenomenon while putting the solver under stress by having strong velocity gradients. The Inputs are $C_s = 0.25$, $\nu_{air} = 1.56 \cdot 10^{-5} m^2.s^{-1}$, $h = 0.015m$, $\sigma = 0.0225$, $\Delta t = 0.001s$, the 3^{nd} order Runge Kutta scheme and the Gaussian regularisation are used. The rings are made of 3 layers each, have $\Gamma = 1m^2.s^{-1}$, $a = 0.05$ and are initially placed one inside the other. The bigger ring has $R = 1m$ while the other has $R = 0.75m$.

The simulation is represented in Figure 9, for a Q-criterion of $20s^{-1}$. The rings follow the back-and-forth motion of the leap-frog. The general toroidal shape of the rings is preserved despite the strong stretching and compression they undergo. This shows the stability of the solver as well as its ability to conserve connections between vortical structures. After $\approx 7s$, the rings start to reach out. At this point, the faster spinning ring drags the slower one, and the structure of the rings sustain strong stretching as they start twisting around each other. The computation of the diffusion term then helps them merge into one as they roll up.

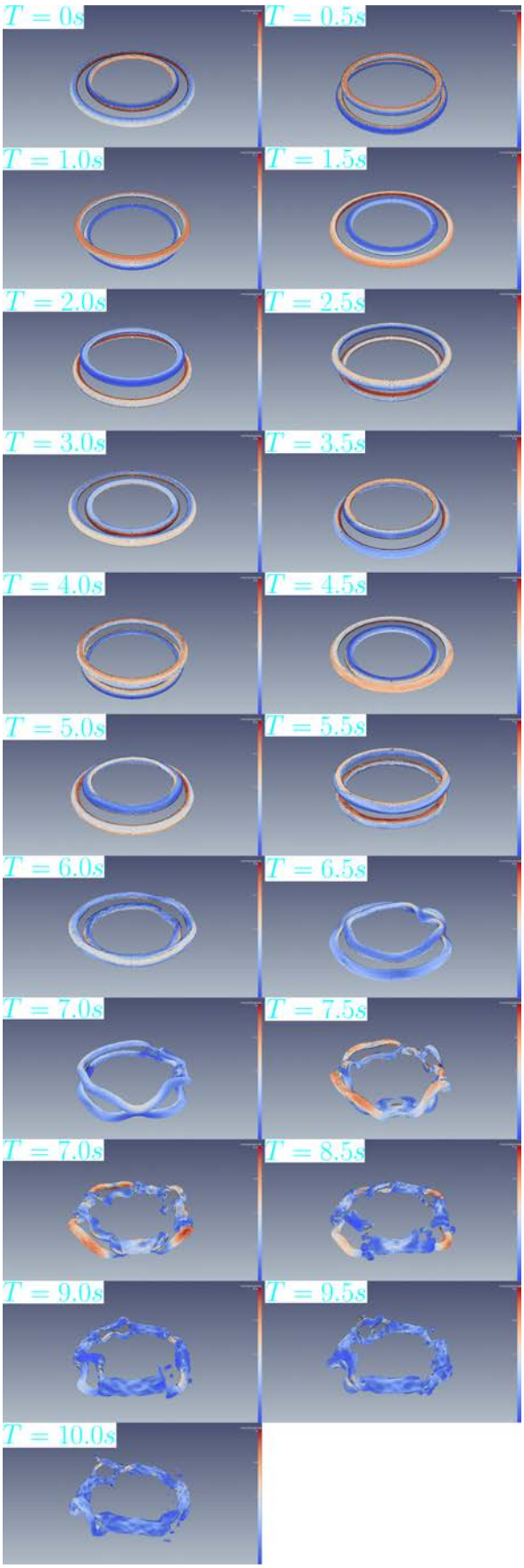

Fig. 9: *Vortex Rings' Leap-Frog Simulation.*

III.5 Rings Fusion

The last case concerns the fusion of two vortex rings. The rings are identical and placed side-by-side, pointing in the same direction. It has observed experimentally[14], that the two rings will merge to form a single (quite deformed) ring. Following the initial fusion of the two rings, the newly formed ring will collapse into two smaller rings. This phenomenon can be replicated by the computing of the viscous term of the vorticity equation.

The inputs are $C_s = 0.25$, $h = 0.001m$, $\sigma = 0.0015m$, $\Delta t = 0.0025s$, the 3^{rd} order Runge Kutta scheme are used and each ring is discretised by 4 layers. The problem is solved using the Gaussian regularisation. The solution is compared with Winckelmans whom applied the HOA regularisation. is used in order to be compared with the HOA's used by Winckelmans who happened to have done the same simulation[17]. Pedrizzetti also carried out this simulation and obtained similar results[11]. Winckelmans pointed out that a lot a layers were necessary to represent the flow near the rings in order to capture the diffusion of vorticity to the outer layers. However, in this study few layers are used thanks to the global redistribution. This scheme allows the vor-

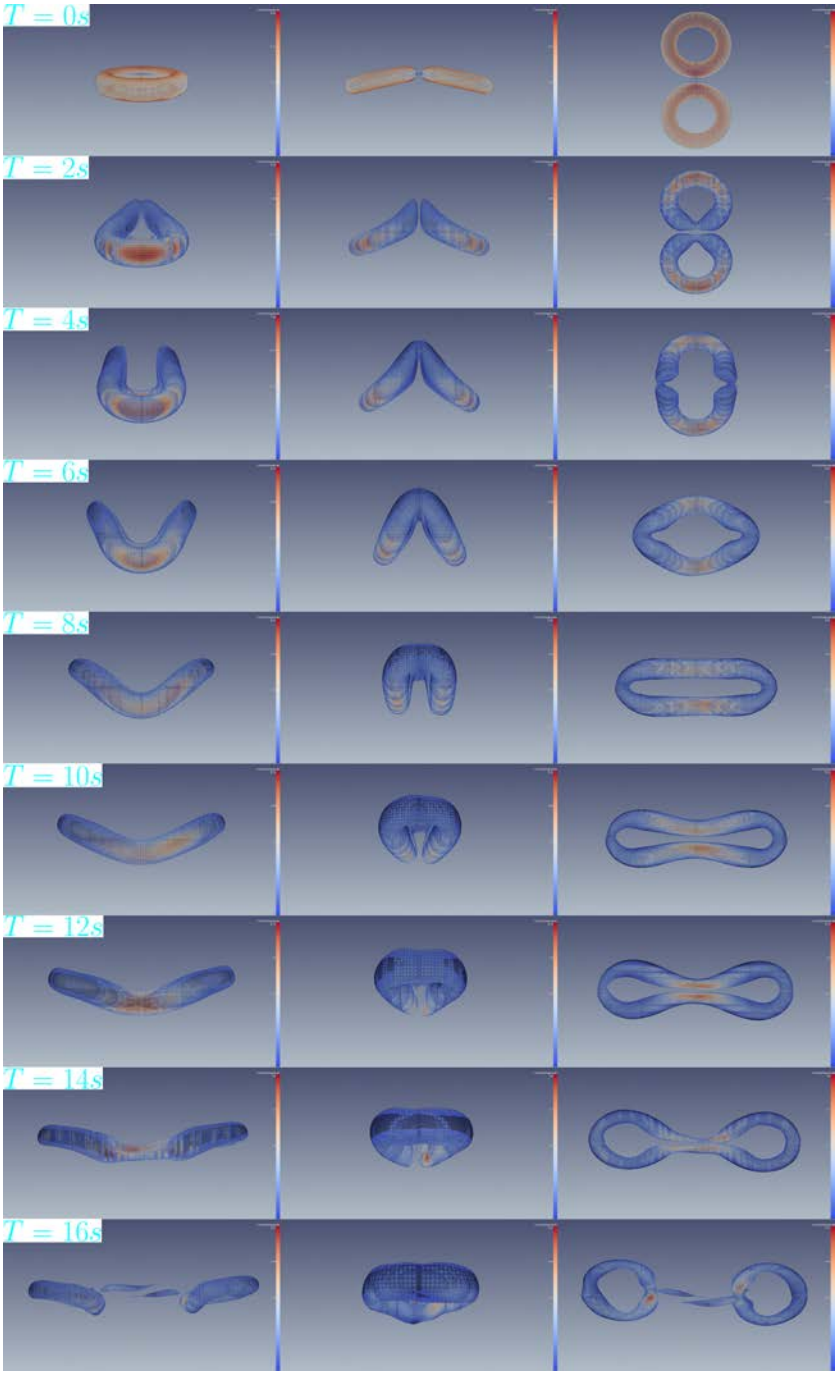

Fig. 10: *Front (left), Side (middle) and Top Views (right) of the Vortex Rings' Fusion by the VPM.*

ticity to spread at its own pace by adding particles around the ring. The small timestep allows to use this scheme every 40 timesteps only. The relaxation scheme is applied after every redistribution with a cutoff of $0.02Hz$. A $||\overrightarrow{\alpha}||$ cutoff was set to $10^{-19}m^3.s^{-1}$ to eliminate particles that do not have enough strength in order not to overload the simulation with unnecessary redistribution.

The physical parameters of the simulation are taken as the averaged values between the two rings from Schatzle's experiments: $\Gamma = 0.001605m^2.s^{-1}$, $R = 0.016575m$, $a = 0.004025$ and $\nu_{water} = 9 \cdot 10^{-7}m^2.s-1$. The rings are initially positioned like in the experiment's, in a '$\wedge$' shape with an angle of $-13.3°$ from the horizontal and put $0.0446m$ apart from each other (center-to-center). The simulation is available in Figure 10, with a Q-criterion of $1s^{-1}$.

The rings merge together at $\approx 5s$. After that, their initial inertia stretch the newly formed ring into an ellipse. Under the influence of the stretching term, the new ring collapses into two large opened rings at $\approx 13s$. Being thrown in opposite directions, the two collapsed and opened rings close themselves to form two whole rings at $\approx 16s$. After that the rings are too thick to split again and end up collapsing on themselves, killing what is left of their vorticity.

This whole phenomenon has been captured during Schatzle's experiment, a visualisation is provided from Schatzle's thesis in Figure 11. The fact that the experiment was much shorter than the simulation can be attributed to a variety of reasons. Firstly, the experiment's rings were translating because of their own self-induced velocity (like in the simulation) but also because of the flow velocity generated by the pistons that created the rings. The parameters of the simulation could also be underestimated. A smaller ring radius a or a higher circulation Γ greatly speeds up the process and make the rings merge and break faster.

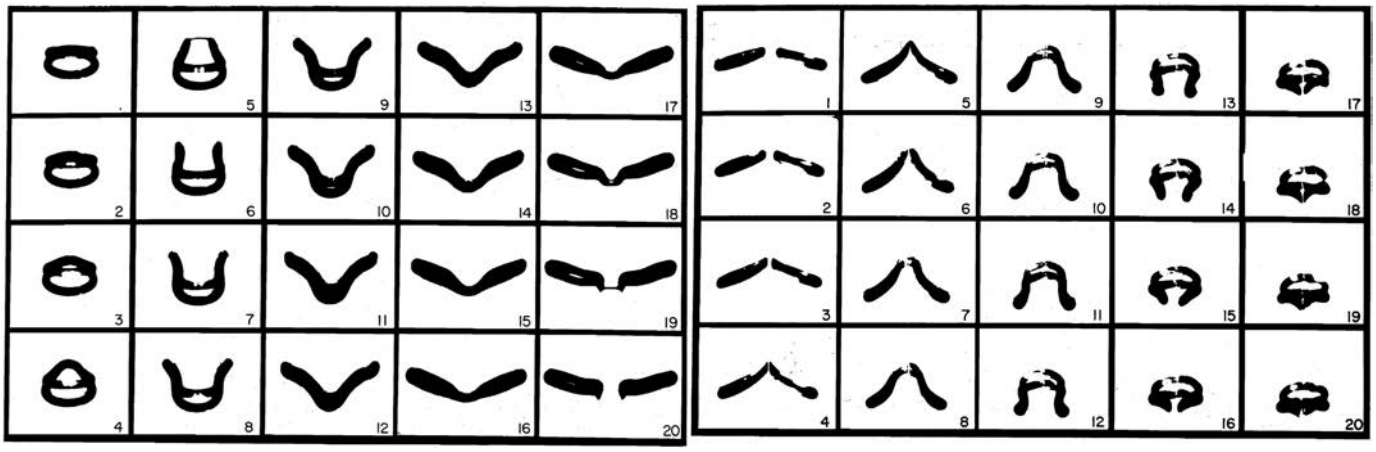

Fig. 11: *Front (left) and Side View (right) of the Vortex Rings' Fusion Experiment by Schatzle[14].*

IV Lifting Line Coupling

IV.1 Modelisation

A Lifting Line (LL) module has been added to the solver. This century-old method remains relevant to this day thanks to its low computational cost and simplicity.

The load on the LL is computed from the effective angle of attack at each of its blade elements. 2D polars are used to get the aerodynamical loads on the LL.

$$\begin{cases} L = \frac{1}{2}\rho_\infty \int u_{rel}^2 c C_l(\alpha_{rel}) dy \\ D = \frac{1}{2}\rho_\infty \int u_{rel}^2 c C_d(\alpha_{rel}) dy \end{cases} \tag{24}$$

The circulation is then recovered from the Kutta-Joukowski Theorem:

$$\overrightarrow{L} = \rho_\infty \int \overrightarrow{u}_{rel} \times \overrightarrow{\Gamma} dy \tag{25}$$

The introduction of a solid in the flow creates vorticity according to Kelvin's Theorem. Two contributions to this vorticity source can be identified:

$$\frac{d\Gamma}{dt} = \frac{\partial \Gamma}{\partial t} + \overrightarrow{u}_m \cdot \nabla \Gamma = 0 \tag{26}$$

These two terms contribute to the generation of vorticity because of the temporal rate of change and the spanwise variation of the circulation on the solid. To respect this, particles are shed along the LL and are set free in the wake[12][16][15][1]. The temporal contribution generates shedding particles, parallel to the LL while the spatial variations contribute to the generation of trailing particles, perpendicular to the LL. In turn, the particles of the wake induce velocities on the LL which affect the α_{rel} and $\overrightarrow{u}_{rel}$ of each blade element. This process is repeated at each timestep until convergence of the circulation is reached. To have large timesteps without destabilising this iteration process, a relaxation scheme is introduced when updating the circulation:

$$\Gamma_{n_{new}} = \Gamma_{n-1} + k_{relax}(\Gamma_{n_{old}} - \Gamma_{n-1}) \tag{27}$$

at the n^{th} iteration. The process is stopped when $\max_{LL}(|\Gamma_n - \Gamma_{n-1}|)$ falls below a given threshold.

IV.2 Elliptical Wing

The VPM has been studied on an elliptical wing. This peculiar geometry offers convenient analytical results providing validation for the LL module.

The wing has a reference chord of $c_0 = 0.34m$, a wingspan of $b = 1.6m$ and its chord repartition is $c(y) = c_0\sqrt{1 - \left(\frac{2y}{b}\right)^2}$. The NACA 0012 airfoil is used for the whole wing. The wing is furthermore untwisted, has neither dihedral nor sweep. Its surface is given by $S = \frac{\pi}{2} c_0 L \approx 0.427m^2$. The specificity of this wing, renowned for being on UK's Spitfires during WWII, is that its shape minimises its induced drag and gives elliptical circulation and lift. The overall aerodynamic coefficients, circulation, induced velocity and induced angle are provided by Prandtl's theory:

$$c_L = \frac{b^2 \pi \alpha_i}{S} = \frac{2F}{\rho_\infty u_\infty^2 S} \tag{28}$$

$$c_D = c_{D_p} + c_{D_i} = \frac{1}{S}\int Cd(y)c(y)dy + \frac{c_L^2 S}{\pi b^2} \tag{29}$$

$$\Gamma(y) = \Gamma_0 \frac{c(y)}{c_0} \tag{30}$$

$$w_i(y) = w_i(0) = -\frac{\Gamma_0}{2b} \tag{31}$$

$$\epsilon(y) = \epsilon(0) = \arctan\left(\frac{\Gamma_0}{2u_\infty b}\right) \quad (32)$$

where $\Gamma_0 = \frac{4F}{\rho_\infty u_\infty b\pi}$ and c_{D_p} is the profile drag. In our case, the overall lift is obtained by taking into account the influence of the induced velocity and angle:

$$F = \frac{1}{2}\rho_\infty \int u_{rel}^2 c \left(C_l \cos(\epsilon) - C_d \sin(\epsilon)\right) dy \quad (33)$$

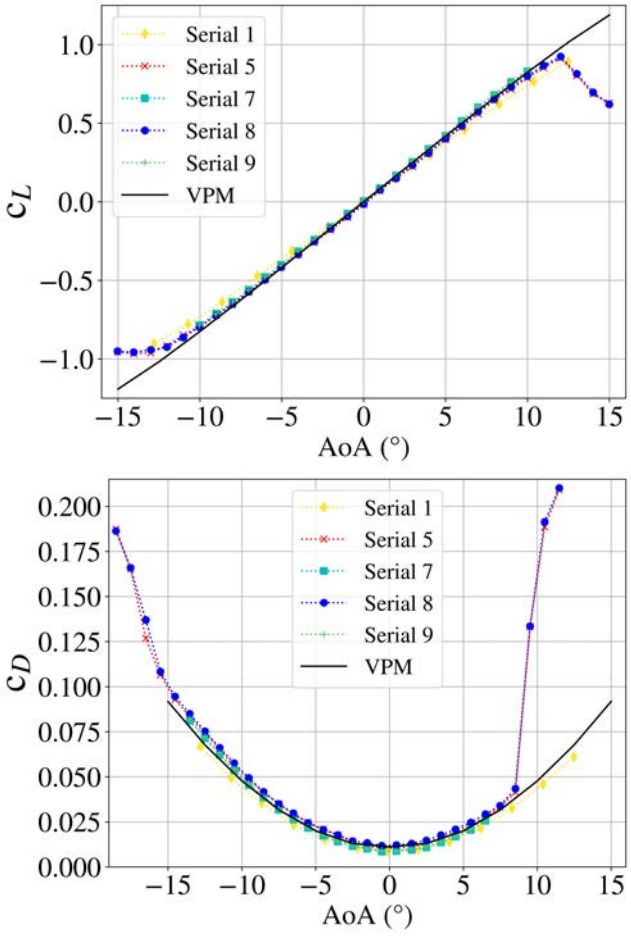

Fig. 12: *Experimental and VPM Polars Comparison.*

Polars have been obtained from the VPM and series of experiments conducted in ONERA's L1 wind tunnel in Meudon. The VPM inputs are $u_\infty = 50m.s^{-1}$, $h = \frac{b}{101} \approx 0.016m$, $\sigma = 2h$, $\Delta t = h/u_\infty$, $k_{relax} = 0.37$, $\nu_{air} = 1,56 \cdot 10^{-5}m^2.s{-}1$, $C_s = 0.15$, the 3^{rd} order Runge Kutta scheme is used, the redistribution is carried out every 11 timesteps with a cutoff of $7,5 \cdot 10^{-11}m^3.s^{-1}$ followed every time by the relaxation scheme with a cutoff of $0.02Hz$. The air density was taken from the ideal gas law at a temperature of 19°C and at standard atmospheric pressure to respect the experimental conditions.

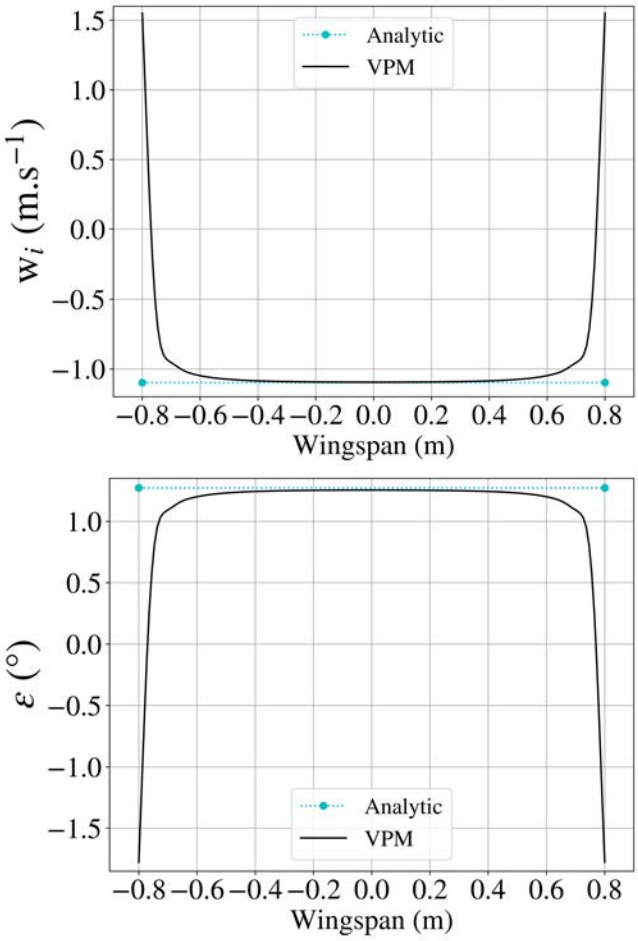

Fig. 13: *Analytical and VPM w_i (top) and ϵ (bottom) Comparison.*

As can be seen in Figure 12, experimental and VPM polars match as long as the AoA is in the linear range of c_L. This is partly due to the

2D polars having trouble representing the stall for high AoA, and the LL requiring small AoA.

A focus is made on the case where $\alpha_0 = 5°$ to confront this result with Prandtl's theory. As one can see from Table:3, the analytical and numerical results concur. The induced velocity w (and thus the induced angle ϵ) is supposed to remain constant for an elliptical wing with an infinite aspect ratio. But as can be seen in Figure 13, it is not the case at the wingtips.

The LL itself depends on having a high aspect ratio to avoid such issues. However modern aircrafts have an aspect ratio going from around 7 to 10. Wingtip vortices play a major part in the loads of the wing and the wake it generates. This causes a small deviation in the circulation at around $|y| = 0.77m$ (see Figure 15). These vorticies can be observed in Figure 14. The case of the elliptic wing tend to downplay this impact on the c_L and c_D because of its rapidly decreasing chord at the wingtips.

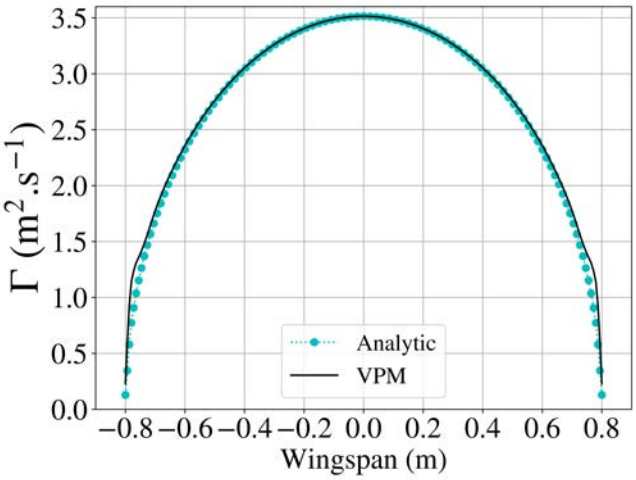

Fig. 15: *Analytical and VPM Circulation Comparison.*

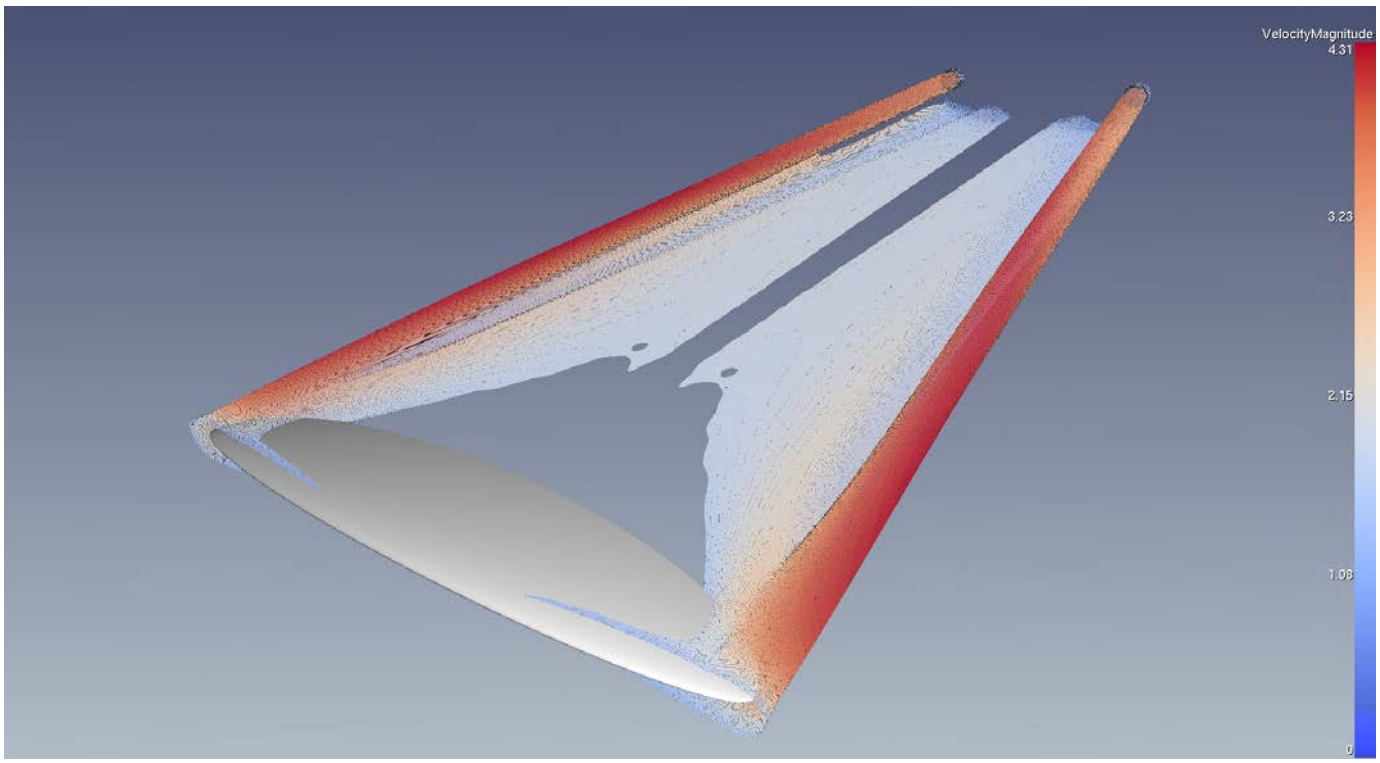

Fig. 14: *Elliptical Wing's Wake for a Q-criterion of* $1s^{-1}$.

V Conclusion

The Vortex Particle Method solver has successfully been implemented and accelerated by a Fast Multipole Method module. A redistribution and a relaxation scheme have also been added to the algorithm to improve its robustness. The solver has first been validated without vorticity sources, comparing its solution to other studies. A Lifting Line module has been added and also validated on an elliptical wing by confronting experimental and analytical results. However, other wings have to be simulated to unsure the sturdiness and versatility of the solver when confronted with unusual geometries or polars. In the future, rotors and propellers will be treated. Indeed they make for perfect tests because of the strong 3D dynamics, stalls, strong velocity gradients, blade twists and strong vorticities generated.

Acknowledgment

We want to thank Christophe Verbeke and Jean-Claude Monnier for the experiments they conducted on the elliptical wing and Didier Bailly for the post-treatment of the experiment's data.

References

[1] E. J. Alvarez and A. Ning. "*High-Fidelity Modeling of Multirotor AerodynamicInteractions for Aircraft Design*". In: *AIAA Journal* 58.10 (Oct. 2020). DOI: 10.2514/1.J059178.

[2] T. Beale and A. Majda. "*Vortex Method. I: Convergence in Three Dimensions*". In: *Mathematics of Computation* 39.159 (July 1982), pp. 1–27. DOI: 10.2307/2007617.

[3] C. Benoit, S. Péron, and S. Landier. "Cassiopee: A CFD pre- and post-processing tool". In: *Aerospace Science and Technology* 45 (2015), pp. 272–283. DOI: 10.1016/j.ast.2015.05.023.

[4] J. Calabretta. "*A Three Dimensional Vortex Particle-Panel Code for Modeling Propeller Airframe Interaction*". Faculty of California Polytechnic State University, June 2010.

[5] C. Greengard. "*Convergence of the Vortex Filament Method*". In: *Mathematics of Computation* 47.176 (Oct. 1986), pp. 387–398. DOI: 10.2307/2008162.

[6] C. He and J. Zhao. "*Modelling Rotor Wake Dynamics With Viscous Vortex Particle Method*". In: *AIAA Journal* 47.4 (Apr. 2009), pp. 902–915. DOI: 10.2514/1.36466.

[7] O. M. Knio and A. F. Ghoniem. "*Numerical Study of a Three-Dimensional Vortex Method*". In: *Journal of Computational Physics* 86 (1990), pp. 75–106. DOI: 10.1016/0021-9991(90)90092-F.

[8] J. R. Mansfield, O. M. Knio, and C. Meneveau. "Dynamic LES of Colliding Vortex Rings Using a 3D Vortex Method". In: *Journal of Computational Physics* 152 (1999), pp. 305–345. DOI: 10.1006/jcph.1999.6258.

[9] E. H. Martin. "*Assessment of Panel and Vortex Particle Methods for the Modelling of Stationary Propeller Wake Wash*". Memorial University of Newfoundland, Oct. 2015.

[10] Mas-Gallic. "*Contribution à l'Analyse Numérique des Méthodes Particulaires*". Université Paris VI, 1987. DOI: 10.15368/theses.2010.104.

[11] G. Pedrizzetti. "*Insight into singular vortex flows*". In: *Fluid Dynamics Research* 10.2 (Aug. 1992), pp. 101–115. DOI: 10.1016/0169-5983(92)90011-k.

[12] G. Pinon et al. "Numerical simulation of the wake of marine current turbines with a particle method". In: *Renewable Energy* 46 (2012), pp. 111–126. DOI: 10.1016/j.renene.2012.03.037.

[13] L. Rosenhead and H. Jeffreys. "The formation of vortices from a surface of discontinuity". In: *Royal Society* 134.823 (1931), pp. 170–192. DOI: 10.1098/rspa.1931.0189.

[14] P. R. Schatzle. "*An Experimental Study of Fusion of Vortex Rings*". California Institute of Technology, 1987. DOI: 10.7907/KK00-ZJ41.

[15] P. Singh. "*Aeromechanics of Coaxial Rotor Helicopters Using the Viscous Vortex Particles Method*". University of Michigan, 2020.

[16] M. Tugnoli et al. "*Mid-fidelity approach to aerodynamic simulations of unconventional eVTOL aircraft configurations*". In: *Aerospace Science and Technology* 115 (2021). DOI: 10.1016/j.ast.2021.106804.

[17] G. S. Winckelmans. "*Topics in vortex methods for the computation of three- and two-dimensional incompressible unsteady flows*". California Institute of Technology, 1989. DOI: 10.7907/19HD-DF80.

[18] R. Yokota et al. "*Fast multipole methods on a cluster of GPUs for the meshless simulation of turbulence*". In: *Computer Physics Communications* 180 (2009), pp. 2066–2078. DOI: 10.1016/j.cpc.2009.06.009.

Appendix

	4 layers	$h = 7,78cm$		$\sigma = 10cm$		5 layers	$h = 6,36cm$	$\sigma = 8,4cm$	6 layers	$h = 5,38cm$	$\sigma = 7,35cm$
Diagnostic	Study	W.	S.	C.	M.	Study	W.	S.	Study	W.	S.
$\lvert\mathcal{I}\rvert$	3,165454	3,213919	3,16545	3,1326	3,274	3,173189	3,215482	3,1785	3,173189	3,215482	3,1785
$E_{div-free}$	1,016773	1,047634	1,01677	1,012922	1,0408	1,010371	1,036526	1,01369	1,010371	1,036526	1,01369
E	1,016694	1,047552	1,01669	1,012823	1,0407	1,010330	1,036491	1,01366	1,010330	1,036491	1,01366
$\mathcal{E}_{div-free}$	60,41207	62,38420	60,4121	63,38210	63,52	57,54908	58,99072	57,6503	57,54908	58,99072	57,6503
$\mathcal{E}$	61,41085	61,34640	61,4109	N/A	N/A	58,30688	58,30524	58,3174	58,30688	58,30524	58,3174
U_R	0,249509	0,26605	0,2496272	N/A	N/A	0,250503	0,26607	0,251092	0,250503	0,26607	0,2510928
dE/dt	-0,12355	-0,1276	-0,1496	-0,1276	N/A	-0,12346	-0,12684	-0,1526	-0,12346	-0,12684	-0,1526

Table 2: *Diagnostics Comparison of three Self-Induced Rings with WINCKELMANS Gérard[17], SINGH Puneet[15], CALABRETTA Jacob[4] and MARTIN Evan[9] for* $\nu = 2,5 \cdot 10^{-3} m^2.s^{-1}$.

	Γ_0 $[m^2.s^{-1}]$	$w_i(0)$ $[m.s^{-1}]$	$\epsilon(0)$ [°]	c_L	c_D	c_{D_i}	c_{D_f}
VPM	3.51418	-1.09523	1.25512	0.418336	0.0200595	0.00929715	0.0113207
Analytical	3.55586	-1.11121	1.27314	0.413433	0.0206178	0.0090805	0.0113207
Relative Error [%]	1,17	1,44	1,4	1,19	2,71	2,39	0.00

Table 3: *Comparison Between Prandtl's Theory and the VPM on the Elliptical Wing for* $\alpha_0 = 5°$.